

Journal of Materials Chemistry A

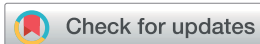
Materials for energy and sustainability

rsc.li/materials-a



ISSN 2050-7488

PAPER



Cite this: *J. Mater. Chem. A*, 2023, **11**, 23249

Design of single-atom catalysts for NO oxidation using OH radicals†

Weijie Yang,^{abc} Liugang Chen,^{abc} Zhenhe Jia,^{abc} Binghui Zhou,^{abc} Yanfeng Liu,^{abc} Chongchong Wu^d and Zhengyang Gao^{*abc}

The catalytic oxidation of NO is an effective route for removing NO. However, achieving high oxidation efficiency of NO at a low temperature remains a great challenge. Therefore, the challenge for NO oxidation was addressed *via* adopting an advanced oxidation method of OH radicals over the emerging single-atom catalysts (SACs). Through spin-polarized density functional theory calculations, the reaction paths of NO oxidation with OH radicals over 8 types of TM–N₄–C SACs were explored. Based on the linear scaling relationship and Brønsted–Evans–Polanyi relationship, a kinetic volcano model of NO oxidation was established using OH adsorption energy as a descriptor. Through screening 3d, 4d, and 5d transition metals of SACs, Fe–N₄–C was found to have the highest reaction rate among them. The energy barrier is only 0.86 eV for the rate-determining step of NO oxidation over Fe–N₄–C, indicating that the catalytic oxidation of NO can efficiently take place at room temperature. Based on the linear relationship of adsorption energy between O and OH, the catalytic reactions of NO oxidation using O₂ and OH radicals were plotted in the unified volcano map with O adsorption energy as the descriptor. Obviously, the catalytic oxidation of NO using OH radicals has a higher activity than that using O₂ for the system of SACs. Furthermore, the catalytic activity origin was analyzed through the electronic properties of SACs, such as Bader charge, electronegativity, and d-band center. This study provides a new approach for the current NO oxidation, which can guide us in the screening of catalysts and experimental preparation work in the future.

Received 30th August 2023
Accepted 1st October 2023

DOI: 10.1039/d3ta05199d

rsc.li/materials-a

1. Introduction

The large amount of nitrogen oxides produced by coal-fired power plants can cause severe pollution to the environment. Among them, NO causes acid rain, rise of temperature, and serious diseases, which seriously affect human life and health.^{1,2} At present, catalytic oxidation is a major technology for NO removal, which can oxidize NO to high-valence products and then remove them.^{3–5} However, the current catalysts used for NO oxidation still need to overcome a large reaction energy barrier, which means that it can only be carried out at a higher reaction temperature. This will consume a large amount of energy and also restrict the development of NO catalytic oxidation technology.⁶ Consequently, it is particularly

significant to investigate catalysts with efficient and high reaction performance at lower reaction temperatures for NO removal.

Several researchers have experimentally prepared diverse materials for the oxidative removal of NO.^{7–9} Li *et al.*¹⁰ developed PdCN by incorporating Pd particles into a C₃N₄ material, and this innovative composite exhibited superior efficacy in purifying NO from the air. Similarly, Yi *et al.*¹¹ successfully harnessed the synergistic advantages of a two-dimensional (2D) structure and heteroatom modification in g-C₃N₄, resulting in improved performance and remarkable stability for catalytic NO removal. There are two technology routes to improve the efficient oxidation of NO: one is to use more powerful oxidants, and the other is to use more active catalysts. Single-atom catalysts (SACs) have been widely utilized to remove air contaminants because of their good reaction performance.^{12–15} Zhu *et al.*¹⁶ synthesized atomically dispersed transition metal phase graphite carbon materials for reducing NO_x. By studying the effects of transition metal types and calcination atmosphere on catalytic activity, it was determined that Mn–SAC loaded on 5% Mn graphite carbon at 275 °C has stable catalytic activity. Its conversion rate of NO_x can reach up to 98%. This also proves that single-atom catalysts have great potential for the oxidation of NO. Hu *et al.*¹⁷ prepared SACs by embedding individual Pd

^aDepartment of Power Engineering, North China Electric Power University, Baoding 071003, Hebei, China. E-mail: yangwj@ncepu.edu.cn; gaozhyan@163.com

^bHebei Key Laboratory of Low Carbon and High-Efficiency Power Generation Technology, North China Electric Power University, Baoding 071003, Hebei, China

^cBaoding Key Laboratory of Low Carbon and High-Efficiency Power Generation Technology, North China Electric Power University, Baoding 071003, Hebei, China

^dCNOOC Research Institute of Refining and Petrochemicals, Beijing 102200, PR China

† Electronic supplementary information (ESI) available. See DOI: <https://doi.org/10.1039/d3ta05199d>

atoms *via* chemical impregnation and calcination. The photocatalytic study of NO was conducted under visible light conditions. Through experiments and DFT calculations, it was found that the addition of Pd atoms promoted the photocatalytic degradation of NO. Previous research results indicate that SACs, as high catalytic activity catalysts, may also have great potential in the oxidative degradation of NO.

Efficient performance has been demonstrated in the catalytic oxidation of NO using O₂ and other oxidants on SACs. For instance, Gao *et al.*¹⁸ studied the reaction of O₂ catalytic oxidation of NO on the (Fe, Co)/N-GN catalyst surface using DFT calculations, and it was concluded that O₂ can easily oxidize NO into NO₂. Through thermodynamic analysis and kinetic analysis, it was found that the Eley–Rideal mechanism is the most advantageous. Although its oxidation energy barrier is only 0.17 eV, its NO₂ desorption energy barrier is 1.5 eV, which also limits the reaction activity of the catalytic process. Si *et al.*¹⁹ conducted research on the oxidation of NO by O₂ using five SACs (Fe, Co, Ni, Cu, and Pt). Their findings revealed that nitrogen doping agents effectively modulate the electronic structure of metal active sites. Furthermore, a notable correlation was observed between the turnover frequency (TOF) value of SACs and the adsorption energy of O. Remarkably, Co-SACs exhibited the most exceptional catalytic performance, boasting a remarkable TOF value of 0.33 s⁻¹, surpassing the rates achieved by traditional NO oxidants. Using DFT calculations and microkinetic modeling, Yang *et al.*²⁰ studied the reaction process of O₂ catalytic oxidation of NO on SACs and derived a dynamic model of volcanic shape. The Fe–N₄–C catalyst was proved to have the best oxidation properties, but its final desorption energy barrier was 1.33 eV. However, traditional oxidant removal technologies for NO mostly require high conversion rates under high-temperature conditions, which consume a large amount of energy. Therefore, it is urgent to find a good oxidant that can spontaneously react at room temperature to promote the development of NO removal technology.

The advanced oxidation method has arisen as a prospective technique for pollutant removal owing to its effective removal of waste, inexpensiveness, and good performance of recoverable products.^{21–24} Among them, the Fenton reaction of H₂O₂ activation to generate OH radicals has attracted increasing attention. The OH radicals have been proven to be effective in removing many pollutants. For instance, Gong *et al.*²⁵ generally investigated the effect of dissolved organic substances (DOMs) on the activation of H₂O₂ on the surface of α -Fe₂O₃ (001) using density functional theory, demonstrating the superior catalytic performance of its Fe site. Through the co-adsorption analysis of DOM molecules and H₂O₂, it was found that the active site can effectively promote the activation of H₂O₂ to generate OH radicals, which can better oxidize DOM molecules. Xia *et al.*²⁶ established a Fe SAC/NC catalyst with abundant FeN₄ sites by the MOF method, which can effectively facilitate the activation of H₂O₂ to generate OH radicals for the oxidation of target organic pollutants. The above-mentioned research studies prove that OH radicals have been used as powerful catalysts in many fields of pollutant oxidation and removal.²⁷ Our previous

research on the oxidation process of NO using H₂O₂ on Fe–N₄–C has shown that the presence of OH radicals can efficiently catalyze the formation of HNO₂ products from NO, which possesses high reaction activity.²⁸ However, it is still unclear how to choose catalysts with better activity, and there is a lack of guidance for catalyst screening. Therefore, we explored the reaction process of NO catalyzed by OH on TM–N₄–C (TM = V–Zn), hoping to find descriptors to filter different SACs.

In this work, we studied the reaction mechanism of NO oxidation using OH on TM–N₄–C (TM = V–Zn) by spin-polarization DFT calculations (ISPIN = 2 of the VASP INCAR). First, we analyzed the adsorption behavior of OH and NO on different SACs and determined that NO oxidation using OH follows the E–R reaction mechanism. Subsequently, we investigated the reaction process of OH catalytic oxidation of NO on all SACs and obtained their energy barrier data. Finally, we obtained a linear relationship between OH and the oxidation energy barrier (E_b) and the desorption energy barrier (E_d). We established a reaction volcano activity plot model for the OH catalytic oxidation of NO using microkinetic modeling and obtained the Fe–N₄–C catalyst is nearest to vertex of the volcano plot. The $E_{\text{ads}}(\text{OH})$ value at the vertex of the volcano plot was determined to be –1.50 eV. Based on the rules that have been discovered, we can regulate the configurations of different catalysts to obtain catalysts with a higher reaction activity and guide subsequent experimental preparation. We analyzed the high reactivity of SAC and OH radicals towards NO, and the low-temperature high conversion reaction of NO oxidation with OH on SACs may be a promising technical direction in the future.

2. Computation and modeling methods

All DFT calculations were performed using the Vienna *Ab initio* Simulation Package software (VASP). The projector augmented wave (PAW)²⁹ method was employed for all computational simulations. The Perdew–Burke–Ernzerhof (PBE)³⁰ functional and the generalized gradient approximation (GGA)³⁰ approach were utilized to calculate relevance interactions. The DFT-D3 framework³¹ was employed to incorporate corrections for van der Waals interactions. Utilizing a $5 \times 3\sqrt{3} \times 1$ graphene sheet with a 20 Å vacuum layer, the catalyst surface was simulated for the SAC model.³² A $2 \times 2 \times 1$ Γ -centered k -point and a 450 eV energy cutoff were used to perform geometric optimization. For each atom, the force constrictor was set to 0.02 eV Å⁻¹. Using a $4 \times 4 \times 1$ k -point grid and an electronic self-consistent calculation threshold of 10⁻⁵ eV,³³ reliable information about the electronic configuration and ground-state energy was obtained. The information of k -point and energy tests is shown in Fig. S1.† Using the Bader charge analytical approach, the analysis of the charges was carried out.³⁴ The stability of the system chemical bonds was examined using the projected crystal orbital Hamiltonian population (pCOHP) approach³⁵ after it was calculated using the LOBSTER software.^{36,37}

The basic steps of the transition state were obtained jointly by the climbing image nudged elastic band (CI-NEB)^{38,39} method

and the improved dimer method (IDM).⁴⁰ A 0.05 eV Å⁻¹ adjustment was made to the necessary force convergence criteria. The minimum value of constraint displacement of ±0.02 Å^{41,42} and the transition state structure are verified by vibration frequency analysis. The calculation equations of binding energy, adsorption energy, energy barrier, and electronegativity were provided in the ESI.†

3. Results and discussion

3.1 Catalyst model

Previous work has demonstrated that four N-doped graphene catalysts in the N-doped approach are easy to fabricate and have good catalytic performance. Therefore, we selected transition metals (TMs) as the active center (TM = V–Zn) (Fig. 1d) and constructed a double-vacancy four N-doped graphene structure as a catalyst for the studies.⁴³ The optimized catalyst structures are shown in Fig. 1a and b. To prove the stability of the constructed catalysts, the binding energies of the catalysts were calculated, as shown in Fig. 1c. It is depicted that the binding energies of the ten catalysts employed were much greater than their reported cohesive energies (as shown by the dashed line in Fig. 1c),⁴⁴ demonstrating the stability of the catalysts.

3.2 Reaction mechanisms of NO oxidation using OH radicals

The valence of N in reactant NO is +2, and hence, it can be oxidized into high-valence products such as NO₂, HNO₂, and HNO₃.⁴⁵ These products are harmless and can be solved

later.^{46,47} Based on our previous research, the most likely reaction product of NO oxidized by OH radical is HNO₂ over Fe–N₄–C, which has the lowest reaction energy barrier.²⁸ Therefore, the pathways of NO oxidized by OH radicals to produce HNO₂ were investigated on SACs. The pathways of NO catalyzed by OH radicals on SACs include both the Langmuir–Hinshelwood (L–H)⁴⁸ and Eley–Rideal (E–R)⁴⁹ reaction mechanisms. According to our calculations, the E–R reaction mechanism existed simultaneously over all single-atom catalysts, and hence, we used it as the reaction mechanism.

3.3 Catalytic oxidation of NO with OH radicals on SACs

According to our calculations, the reaction pathway is similar on all SACs. Therefore, we take the Fe–N₄–C catalyst as one of the examples to provide a detailed introduction of NO oxidation at the catalyst (Fig. 2a). First, the OH radical preferentially adsorbs onto the TM of the SAC, becoming IM0 intermediate (OH radical adsorption on the catalyst surface). Then, NO molecules adsorb onto OH to form the state IS1. As the reaction progresses, NO molecules begin to attack the Fe–O bond. The Fe–O bond gradually breaks and forms a HONO intermediate that adsorbs both O and N onto the catalyst until the Fe–O bond is completely broken, ultimately generating the final product HNO₂. The energy barrier E_b of this process is 0.24 eV, and it will release 0.62 eV of energy during the whole reaction process. The resulting product HNO₂ will be desorbed from the catalyst surface, and the entire reaction process is completed. The desorption energy barrier E_d for HNO₂ on Fe–N₄–C is 0.86 eV.

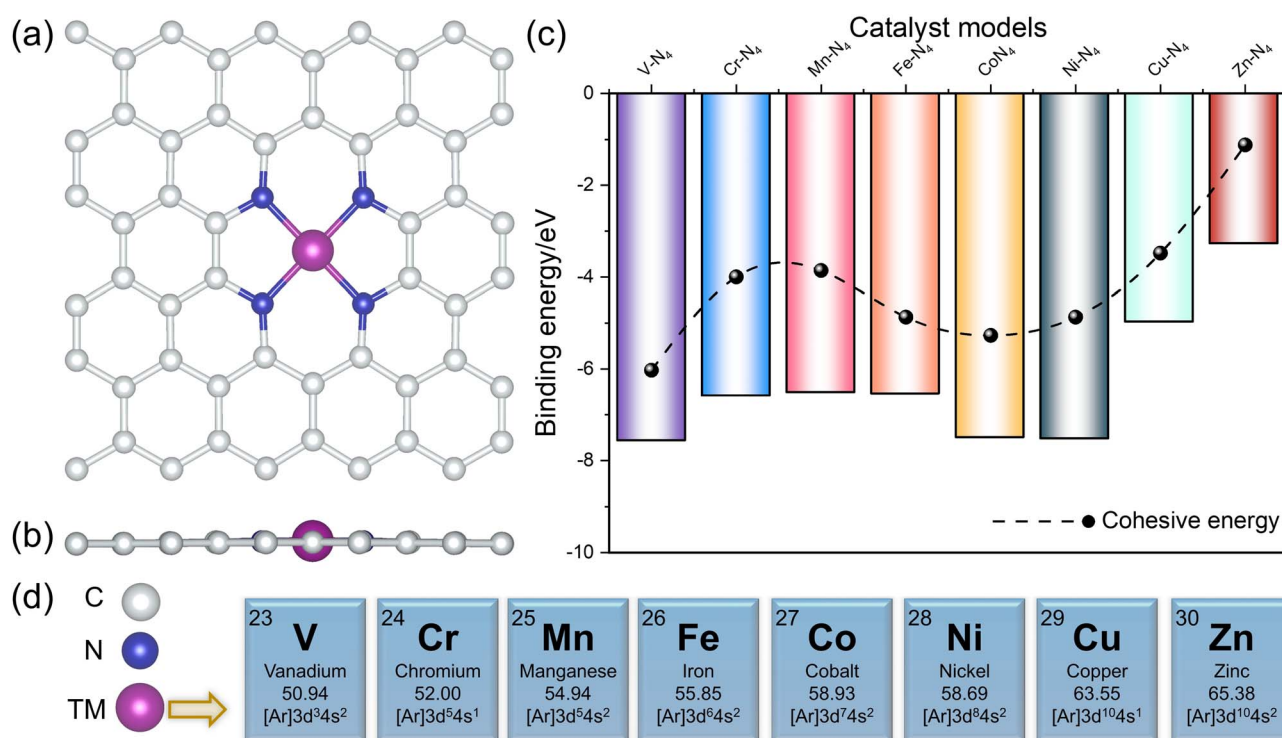


Fig. 1 (a) Vertical and (b) lateral views of the TM–N₄–C catalysts. (c) Calculated binding energies and cohesive energies of 8 SACs. (d) The 3d single TM atoms (TM = V, Cr, Mn, Fe, Co, Ni, Cu, and Zn) taken into consideration for this study. C, N, and TM atoms are represented by gray, blue, and purple colors, respectively.

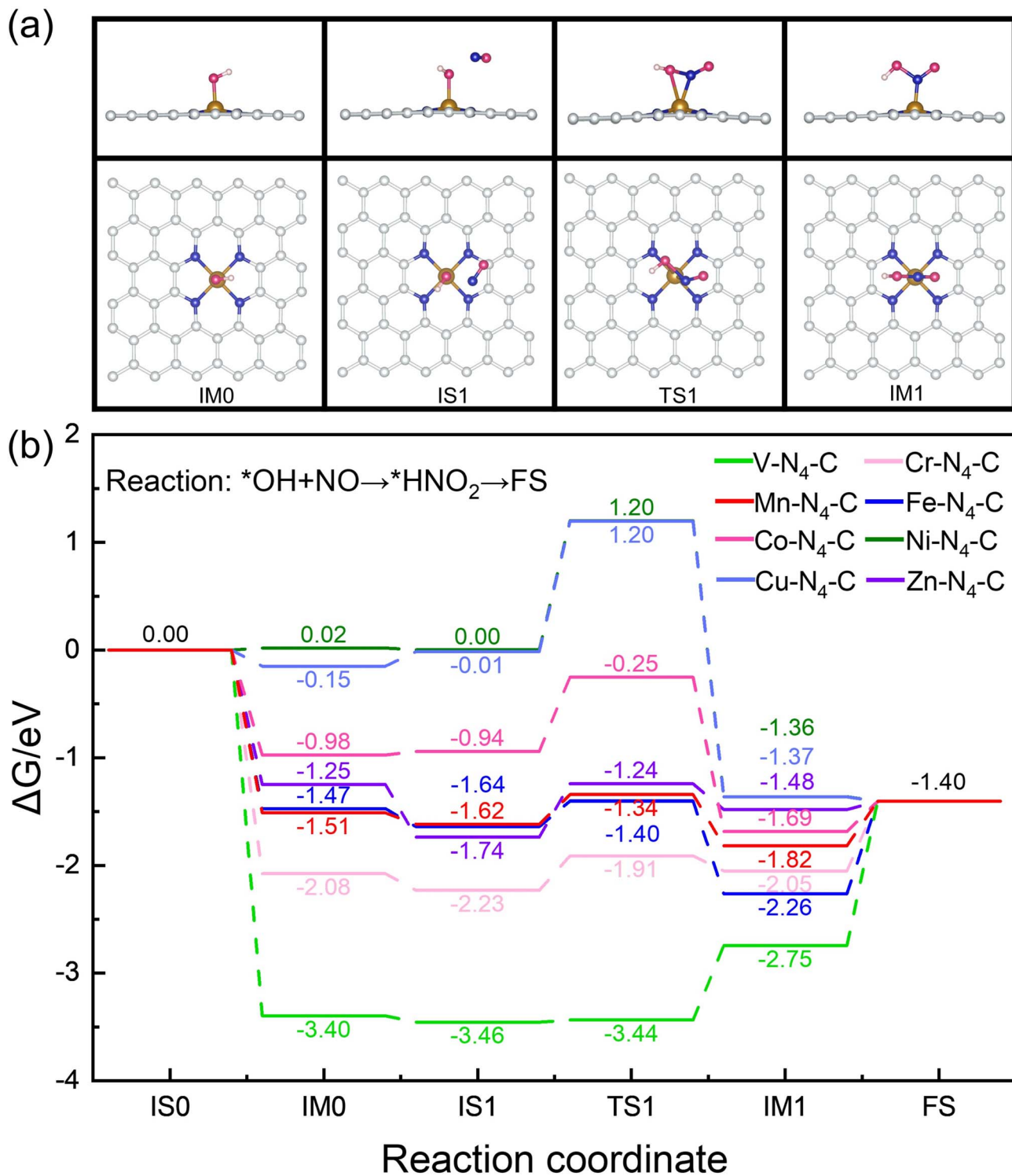


Fig. 2 (a) Instance of the processes of NO oxidation using OH at Fe-N₄-C. (b) Energy variation diagram of the reaction process on 8 types of SACs. The IS0 and FS are catalyst structures. C, N, O, H, and Fe atoms are represented in gray, blue, red, pink, and brown, respectively.

The reaction processes of NO oxidation catalyzed by OH radicals on other SACs are shown in Fig. S2–S8.† Previously, traditional single-atom catalysts mainly used catalysts such as O₂ for NO catalytic oxidation, with a rate-determination step (RDS) energy barrier of up to 1.33 eV⁵⁰ on the Fe-N₄-C catalyst. The NO oxidation energy barrier on (Fe, Co)/N-GN is as high as 1.50 eV.¹⁸

The reaction process of NO oxidation using OH in this work greatly reduces the reaction energy barrier (0.86 eV) compared to traditional oxidants, making the reaction easier to occur and has better development prospects and advantages. Due to the unique properties of Sc-N₄-C and Ti-N₄-C catalysts, as shown in Fig. S9,† we did not consider employing these two catalysts

for the OH catalytic oxidation of NO. After calculating all reaction pathways, we sorted out the imaginary frequencies of the transition state of different reaction processes, as shown in Table S1.†

To analyze the energy changes of the entire reaction process more intuitively, we set the sum energy of an OH radical, NO molecule, and the catalyst surface to a zero-energy state. After conducting proton conservation for each intermediate state, the energy of each intermediate state is determined relative to the ground state. This enables the construction of an energy step diagram depicting the reaction process. Fig. 2b presents the energy changes of the process on eight catalysts. Through the comparison of the reaction barrier E_b and the desorption barrier E_d , all catalysts can be divided into two categories. The first is that the reaction energy barrier is higher than the desorption energy barrier, including Co- N_4 -C, Ni- N_4 -C, Cu- N_4 -C, and Zn- N_4 -C. For this type of catalyst, the activity of the entire reaction process depends on the reaction barrier. The second type is that the reaction energy barrier is higher than the desorption energy barrier, including V- N_4 -C, Cr- N_4 -C, Mn- N_4 -C, and Fe- N_4 -C. On the surface of these catalysts, their reaction barriers tend to be small, but their overall activity is reduced due to their higher energy barriers of the desorption process. Through the above-mentioned analysis, there is an interesting rule that a catalyst with good performance must have moderate reaction energy barriers and desorption energy barriers, otherwise it will affect its overall activity. This also provides us with an idea for building a volcano map model of OH catalytic oxidation of NO.

3.4 Correlation analysis

The reaction kinetics may be connected to the basic thermodynamics of catalytic reactions in the catalytic field.^{51,52} Here the linear relationship between the adsorption energy of OH radicals at the catalyst and the reaction energy barrier (E_b) and desorption energy barrier (E_d) is explored. As shown in Fig. 3a, it is observed that the adsorption energy of OH radicals and E_b have a positive connection. With the decrease in the adsorption energy of OH radicals, E_b at the catalyst increases. Fig. 3b shows the fitting relationship between the desorption energy barrier E_d and the OH adsorption energy. There is a negative correlation between the two, and E_d decreases with the decrease of OH adsorption energy. Through the above analysis, it is interesting that increasing the adsorption energy of OH radical can reduce the reaction energy barrier E_b , but the desorption energy barrier will also increase, thereby affecting the overall activity. Therefore, to regulate the activity of the catalyst, we should control the adsorption energy of OH radicals within a reasonable range.

O₂ is a highly active oxidant commonly used in our previous research on NO catalytic oxidation,^{53,54} and the relationship between the adsorption energy of O and the OH radicals was explored to further investigate NO catalytic oxidation. After obtaining a good linear relationship between the OH adsorption energy and both E_b and E_d , we fitted the OH adsorption energy with the O adsorption energy. Interestingly, it is depicted in Fig. 3c that a significant positive association exists between

the adsorption energies of O and OH radicals. Regarding the data on the O₂ catalytic oxidation of NO over single-atom catalysts, we drew on previous work²⁰ which employed O₂ for NO catalytic oxidation over SACs and established the volcano plot model. Meanwhile, a linear relationship also exists between the adsorption energy of O and the energy barrier of NO oxidation with OH radicals (Fig. S10†). In summary, the characteristics of NO oxidation with OH radicals can be referred from the adsorption of O radicals, providing a new research direction to describe the activity of NO catalytic oxidation with OH radicals by calculating the adsorption energy of O.

In addition, we also investigated the effect of the adsorption energies of OH radicals and HNO₂ on the overall activity of different catalysts (Fig. 3d). It was found that for highly active catalysts such as Fe- N_4 -C, Mn- N_4 -C, Co- N_4 -C, and Zn- N_4 -C, the adsorption energy of OH radicals on these catalysts is close to -1.50 eV. The closer the adsorption energy of the OH radical on the catalysts to the middle (-1.50 eV), the better the catalytic activity. However, for the product HNO₂, it does not follow the same rule as the OH radical. Taking the example of the Fe- N_4 -C SAC, although it has the highest activity among the catalysts investigated, its adsorption strength for HNO₂ is relatively high, suggesting that describing the activity of the catalyst only using the adsorption energy of HNO₂ is not appropriate. To improve catalyst activity, the adsorption strength of the catalyst for HNO₂ should be reduced *via* adjusting the coordination of different catalysts.

3.5 Microkinetic analysis

Based on the above-mentioned analysis results, there is a significant linear relationship between the adsorption energy of OH radicals and both E_b and E_d in the reaction process. Therefore, the adsorption energy of OH radicals can serve as a good descriptor to fit the activity of the catalyst. Here, we use the Sabatier analysis to determine the possible maximum rate,^{55,56} to effectively measure the catalytic ability of the catalyst itself. To be practical, a volcano activity plot was established under the conditions of $T = 400$ K and $P_{H_2O_2} = 0.05$ bar. As shown in Fig. 4a, a volcano activity plot model was developed for NO oxidation using OH radicals. It is depicted that the activity of the catalysts in the left region of the peak is influenced by the desorption energy of the product, whereas the right region is determined by the NO oxidation.⁵⁷ The Fe- N_4 -C catalyst is nearest to the vertex of the volcano plot, corresponding to the OH radical adsorption energy of -1.50 eV. Hence, the closer the OH adsorption energy of different catalysts to -1.50 eV, the higher the theoretical rate of their OH catalytic oxidation of NO. On this basis, we also calculated the OH adsorption energy on 4d and 5d SACs of the same family as V-Zn and obtained the theoretically predicted values of their rates (Fig. 4b). It can be seen that Fe- N_4 -C still exhibits the best performance among these 24 types of SACs, further demonstrating that Fe- N_4 -C still has excellent catalytic activity for NO oxidation.

As a linear relationship between the adsorption energy of OH radicals and the adsorption energy of O on SACs was obtained, the adsorption energy of O radical was used as a descriptor to fit

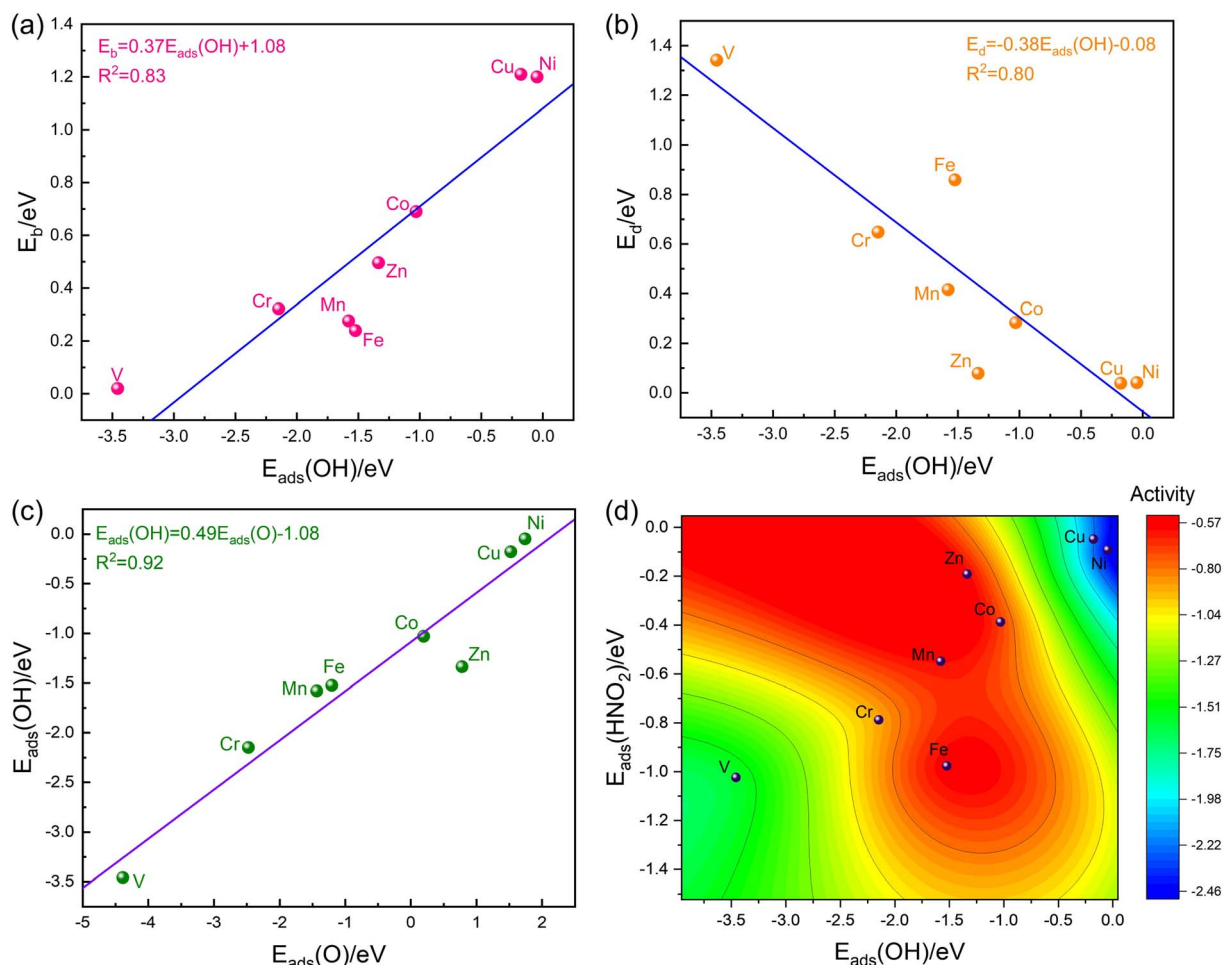


Fig. 3 Correlation analyses of (a) E_b vs. $E_{\text{ads}}(\text{OH})$, (b) E_d vs. $E_{\text{ads}}(\text{OH})$, and (c) $E_{\text{ads}}(\text{OH})$ vs. $E_{\text{ads}}(\text{O})$. (d) The 2D volcano activity model serving as a function of the adsorption energy of OH and HNO_2 .

the active volcano plot of NO oxidation using OH. In addition, the activity volcano plot of using O_2 and OH radicals to catalytic oxidation of NO was also compared in Fig. 4c. It is illustrated that the activity of using O_2 and OH radicals to catalyze the oxidation of NO follows the same trend: both having an active peak, and Fe- N_4 -C is nearest to the vertex of the volcano plot. Compared with the O_2 catalytic oxidation of NO SACs,^{20,58} OH catalytic oxidation of NO has higher activity and can have higher reaction rates at lower reaction temperatures. For the reaction pathway of NO oxidation using OH and O_2 , their rate-determined step energy barriers are those of the product desorption process. For the OH catalytic oxidation of NO, the energy barrier for HNO_2 desorption is 0.86 eV, and for the O_2 catalytic oxidation of NO, the energy barrier for NO_2 desorption is 1.33 eV, which indicates that the upper limit of the catalyst activity is the energy barrier for the desorption of the products, and in the future, we can adjust the structure of the catalysts in order to reduce the energy barrier for the desorption of the products to obtain higher activity catalysts. This also provides a new approach and method for the research of removing NO. In addition, we also explored the difference between the OH radical adsorption energy on these 24 SACs and the

corresponding OH radical adsorption energy at the peak of the volcano plot to evaluate the catalytic activity of different SACs, as shown in Fig. 4d. It further confirmed that catalysts distributed around Fe- N_4 -C often have high catalytic performance.

Meanwhile, we compared the energy barriers in this study with previous studies on the NO oxidation process (Fig. 4e). It can be seen that the energy barriers for the NO oxidation process were relatively high before, and the reaction could only take place at higher temperatures. The reaction process of OH oxidation was used in this work, and the energy barrier data of most catalysts are below 0.96 eV, indicating that the reaction process we studied can have high reaction activity at room temperature.^{59,60}

3.6 Electronic characteristics

Electronic properties are an important factor impacting the activity of SACs.^{61,62} To better control the strength of OH radical adsorption energy at different SACs, we calculated the Bader charge, electronegativity X , and d-band center properties of different SACs. Fig. 5a shows the fitting relationship between Bader charges and OH radical adsorption energy on 28 SACs, and we can see that there is a clear linear relationship between

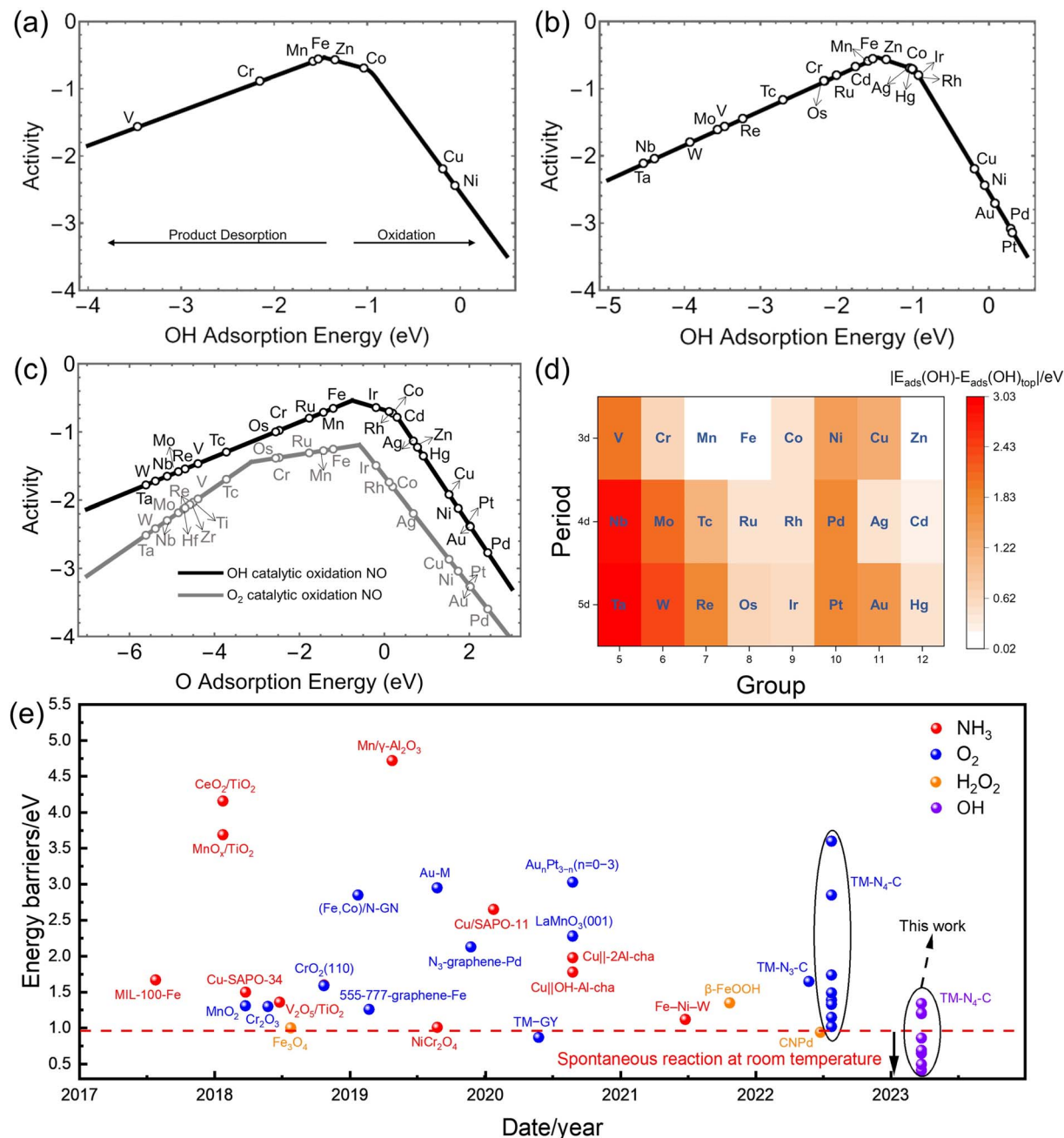


Fig. 4 (a and b) Volcano plots as a function of OH adsorption energy with (a) 8 SACs explicitly analyzed in this study and (b) 24 TM-N₄-C SACs. (c) Volcano plot models for NO oxidation by OH and O₂ using O adsorption energy as descriptors, respectively. (The gray line represents the reaction process of NO oxidation using O₂.) (d) Activities on SACs are predicted using a heat map. (e) Scatterplot compared with previous literature NO reaction energy barrier data.

the two. In addition, we calculated the electronegativity X of 30 SACs and found that there was also an obvious linear relationship between X and OH radical adsorption energy (Fig. 5b). Moreover, the d-band center of TM atoms is also an important indicator for describing the activity of SACs. As shown in Fig. 5c, the d-band centers of 22 SACs were estimated. There is a clear linear relationship between the d-band centers of various metals during the same period and their OH radical adsorption energy. Because there is no significant linear relationship

between the d-band center and adsorption energy of OH radical on all SACs, we delved into the interaction between different d orbitals of TM and OH radical adsorption energy. As shown in Fig. 5d, there is a clear linear relationship between the d_{z²} orbital of TM and the OH radical adsorption energy.

Through the above analysis, we found that for the Fe-N₄-C catalyst nearest to the peak of the volcano plot, its RDS barrier is the desorption of HNO₂, which greatly limits its activity. Therefore, crystal orbital Hamiltonian population (COHP)⁶³ and

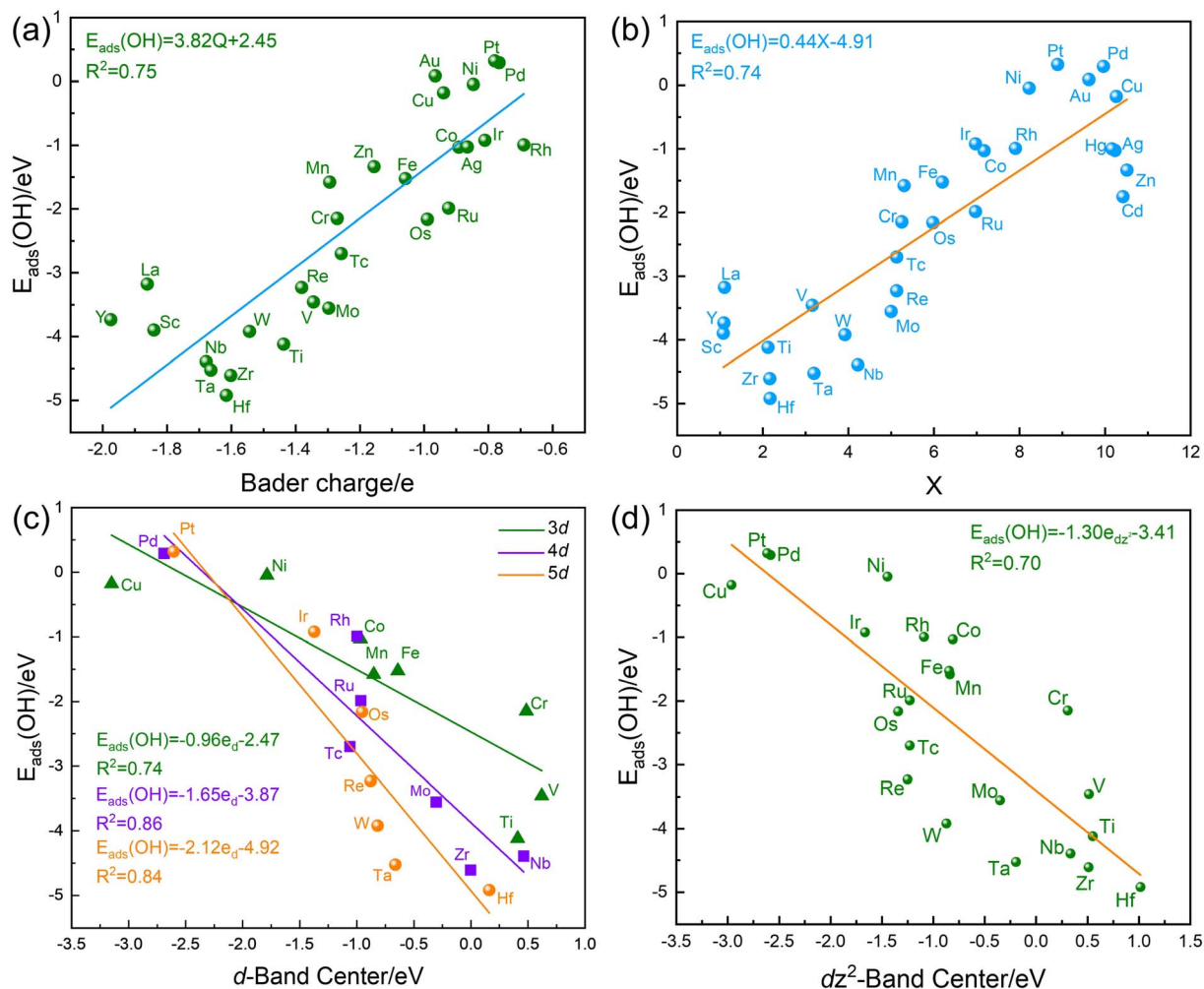


Fig. 5 Linear correlations of (a) $E_{\text{ads}}(\text{OH})$ vs. Bader charge. (b) $E_{\text{ads}}(\text{OH})$ vs. electronegativity (X). (c) $E_{\text{ads}}(\text{OH})$ vs. d-band center, and (d) $E_{\text{ads}}(\text{OH})$ vs. d_{z^2} -band center.

electronic density difference (EDD)⁶⁴ methods were used to analyze the binding strength between different SACs and the product HNO_2 , with an objective to reveal the inherent reasons why different catalysts are difficult to desorb at the micro level. Fig. 6a and b shows the COHP analysis between HNO_2 and the catalyst surface on the Fe- N_4 -C and Cu- N_4 -C catalysts we analyzed. Through COHP analysis, we found that for the Fe- N_4 -C system, the value of its antibonding molecular orbital was very small, which led to a strong interaction between Fe and HNO_2 molecules of -3.92 eV. Therefore, it is crucial to reduce the desorption energy to achieve product desorption, thereby reducing the overall activity of the catalyst. However, for Cu- N_4 -C and other catalyst systems with weak adsorption, their antibonding molecular orbital values are large, resulting in a very small bond strength between the catalyst and HNO_2 , which is only -0.23 eV. The small desorption energy results in the easier subsequent HNO_2 desorption process. The COHP analyses of other SACs are shown in Fig. S11.†

At the same time, to analyze the reasons for the bonding strength between different SACs and HNO_2 from the micro-electronic level, we also made EDD analyses between different

SACs and HNO_2 (Fig. 6c and d). The yellow area gains electrons, while the blue area provides electrons. For Fe- N_4 -C, the Fe atom is surrounded by a cyan region, providing electrons,⁶⁵ and most of the electrons flow toward the HNO_2 molecule. For Cu- N_4 -C, the number of electrons provided by the Cu atom is smaller than those of the Fe atom, and a portion flows towards the surrounding coordination N atoms. Therefore, HNO_2 molecules can obtain a larger number of electrons over the Fe- N_4 -C catalyst, leading to a much greater interaction force between Fe- N_4 -C catalyst and HNO_2 than Cu- N_4 -C. The EDD analyses of other SACs are shown in Fig. S12.† Meanwhile, the statistics on the charge change and bonding bond length between different SACs and HNO_2 were counted as shown in Table S2.†

4. Conclusion

In conclusion, the reaction pathways of NO oxidation using OH radicals on 8 types of 3d TM SACs were systematically analyzed. The reaction kinetics and thermodynamics were examined using the DFT computations. The activity of Fe- N_4 -C is the

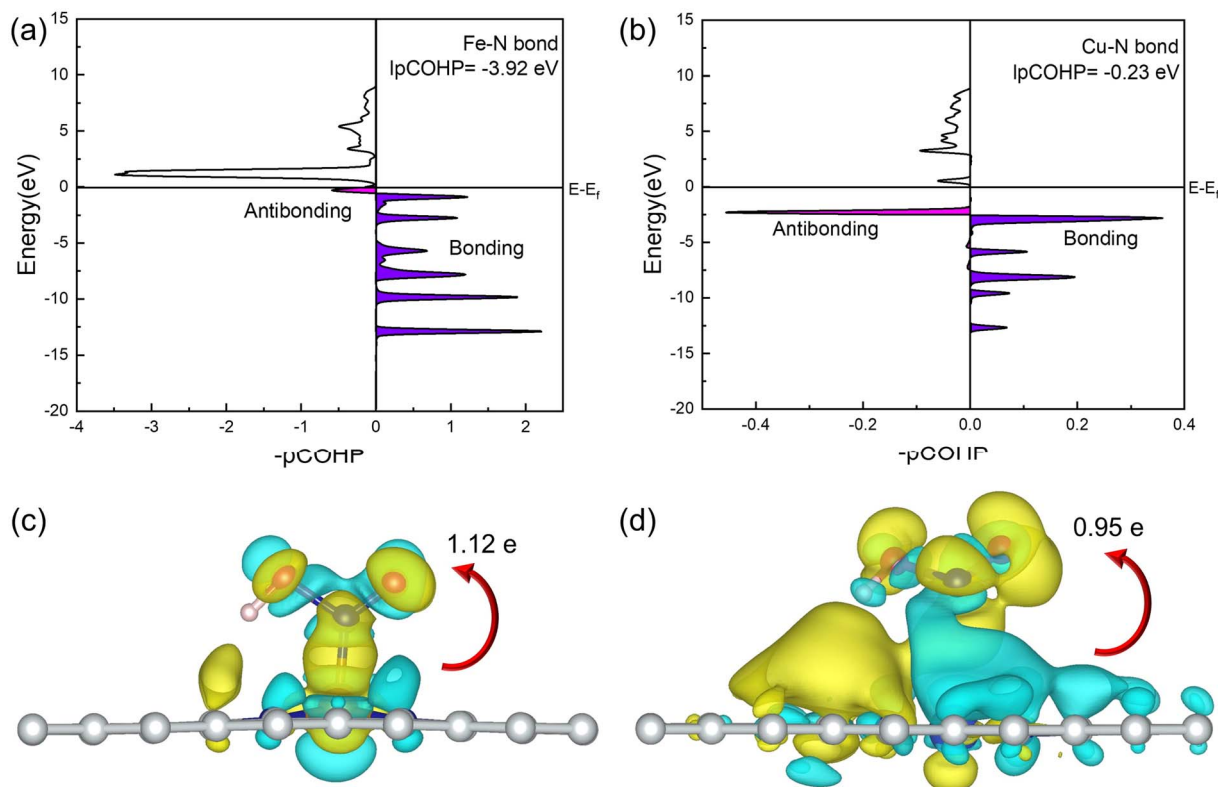


Fig. 6 COHP analysis between different SACs and HNO_2 : (a) Fe- N_4 -C and (b) Cu- N_4 -C. Electronic density difference between different SACs and HNO_2 : (c) Fe- N_4 -C and (d) Cu- N_4 -C. Contour lines in the plots are drawn at $0.001 \text{ e } \text{\AA}^{-3}$ intervals. Yellow and cyan areas represent electron gain and loss, respectively. Gray, blue, red, and pink spheres represent C, N, O, and H, respectively.

greatest among all the catalysts investigated. For the rate-determining step, its energy barrier is only 0.86 eV over Fe- N_4 -C, indicating that the catalytic oxidation of NO can be effectively carried out at room temperature. By analyzing the thermodynamic and kinetic relationships, we found that OH radical adsorption energy can serve as a descriptor for describing catalyst activity. Moreover, based on the microkinetic modeling method, a volcano plot model was derived. The rates of 24 SACs were simulated through the volcano plot, indicating that Fe- N_4 -C was nearest to the vertex of the volcano plot, which showed the highest reaction activity among the 3d, 4d, and 5d SACs we studied. Moreover, $E_{\text{ads}}(\text{OH})$ on the SACs corresponding to the vertices of the volcanic map is -1.50 eV . In comparison with the O_2 catalytic oxidation NO process, we found that OH radicals have obvious advantages in catalytic activity. In addition, through the analysis of Bader charge, electronegativity, and d-band center, the linear correlation between activity and electronic structure was identified. Consequently, the OH radical adsorption energy of the catalyst can be predicted through the electronic properties of the catalyst structure to regulate the activity of the catalyst. We also used COHP and EDD methods to analyze why the products on Fe- N_4 -C catalysts are difficult to desorb from the microelectronic level, to regulate them later. We hope that our research can provide a new approach for pollutant removal and a new theoretical strategy for finding catalysts with better activity for NO oxidation in the future.

Conflicts of interest

There are no conflicts to declare.

Acknowledgements

This work was funded by the National Natural Science Foundation of China (No. 52176104 and 52006073).

References

- 1 J. Dong, Z. Gao, W. Yang, A. Li and X. Ding, *Appl. Surf. Sci.*, 2019, **480**, 779–791.
- 2 F. Cao, S. Su, J. Xiang, P. Wang, S. Hu, L. Sun and A. Zhang, *Fuel*, 2015, **139**, 232–239.
- 3 R. B. Getman and W. F. Schneider, *ChemCatChem*, 2010, **2**, 1450–1460.
- 4 W. Chen, S. Yang, H. Liu, F. Huang, Q. Shao, L. Liu, J. Sun, C. Sun, D. Chen and L. Dong, *Environ. Sci. Technol.*, 2022, **56**, 10442–10453.
- 5 W. Yang, B. Zhou, Y. Zhang, J. Ren, C. Wu, I. D. Gates, Y. Liu and Z. Gao, *Mol. Catal.*, 2022, **533**, 112769.
- 6 W. Chen, Z. Qu, W. Huang, X. Hu and N. Yan, *Fuel*, 2016, **166**, 179–187.
- 7 L. Han, J. Huang, J. Zhan, X. Zhang, S. Wang and H. Chen, *Adv. Sustainable Syst.*, 2023, **7**, 2200009.

- 8 X. Li, Z. Hu, Q. Li, M. Lei, J. Fan, S. A. C. Carabineiro, Y. Liu and K. Lv, *Chem. Commun.*, 2020, **56**, 14195–14198.
- 9 Y. Duan, Y. Wang, L. Gan, J. Meng, Y. Feng, K. Wang, K. Zhou, C. Wang, X. Han and X. Zhou, *Adv. Energy Mater.*, 2021, **11**, 2004001.
- 10 K. Li, Y. He, P. Chen, H. Wang, J. Sheng, W. Cui, G. Leng, Y. Chu, Z. Wang and F. Dong, *J. Hazard. Mater.*, 2020, **392**, 122357.
- 11 J. Yi, J. Liao, K. Xia, Y. Song, J. Lian, X. She, Y. Liu, S. Yuan, F. Dong, H. Xu and H. Li, *Chem. Eng. J.*, 2019, **370**, 944–951.
- 12 Y. Zhang, R. Yang, H. Li and Z. Zeng, *Small*, 2022, **18**, 2203759.
- 13 H. Li, B. Yu, Z. Zhuang, W. Sun, B. Jia and T. Ma, *J. Mater. Chem. A*, 2021, **9**, 4184–4192.
- 14 J. Liu, G. Zhang, K. Ye, K. Xu, Y. Sheng, C. Yu, H. Zhang, Q. Li, Z. Liang and K. Jiang, *Chem. Commun.*, 2023, **59**, 611–614.
- 15 W. Yang, B. Zhou, Z. Jia, C. Wu, L. Wei, Z. Gao and H. Li, *ChemCatChem*, 2022, **14**, e202201016.
- 16 H. Zhu and R. Wang, *J. Mater. Chem. A*, 2023, **11**, 3464–3470.
- 17 L. Hu, T. Wang, Q. Nie, J. Liu, Y. Cui, K. Zhang, Z. Tan and H. Yu, *Carbon*, 2022, **200**, 187–198.
- 18 Z. Gao, X. Liu, A. Li, X. Li, X. Ding and W. Yang, *Mol. Catal.*, 2019, **470**, 56–66.
- 19 C. Si, M. Yang and B. Li, *J. Phys. Chem. C*, 2022, **126**, 18275–18281.
- 20 W. Yang, Y. Feng, X. Chen, C. Wu, F. Wang, Z. Gao, Y. Liu, X. Ding and H. Li, *J. Environ. Chem. Eng.*, 2022, **10**, 108744.
- 21 Z. Cheng, L. Ling, Z. Wu, J. Fang, P. Westerhoff and C. Shang, *Environ. Sci. Technol.*, 2020, **54**, 11584–11593.
- 22 C. Weng, Y.-H. Chuang, B. Davey and W. A. Mitch, *Environ. Sci. Technol.*, 2020, **54**, 12593–12601.
- 23 S. Sharma, V. Dutta, P. Raizada, A. Hosseini-Bandegharai, P. Singh and V.-H. Nguyen, *Environ. Chem. Lett.*, 2021, **19**, 271–306.
- 24 V. Hasija, A. Kumar, A. Sudhaik, P. Raizada, P. Singh, Q. Van Le, T. T. Le and V.-H. Nguyen, *Environ. Chem. Lett.*, 2021, **19**, 2941–2966.
- 25 B. Gong, C. Ku, H.-Q. Yu and P. H. L. Sit, *J. Phys. Chem. C*, 2021, **125**, 8508–8517.
- 26 P. Xia, Z. Ye, L. Zhao, Q. Xue, S. Lanzalaco, Q. He, X. Qi and I. Sirés, *Appl. Catal., B*, 2023, **322**, 122116.
- 27 K. Li, W. Zhou, X. Li, Q. Li, S. A. C. Carabineiro, S. Zhang, J. Fan and K. Lv, *J. Hazard. Mater.*, 2023, **442**, 130040.
- 28 W. Yang, L. Chen, B. Zhou, Z. Jia, X. Liu, Y. Liu, H. Li and Z. Gao, *J. Phys. Chem. C*, 2023, **127**, 13011–13020.
- 29 J. P. Perdew, K. Burke and M. Ernzerhof, *Phys. Rev. Lett.*, 1996, **77**, 3865–3868.
- 30 G. Kresse and D. Joubert, *Phys. Rev. B: Condens. Matter Mater. Phys.*, 1999, **59**, 1758–1775.
- 31 S. Grimme, J. Antony, S. Ehrlich and H. Krieg, *J. Chem. Phys.*, 2010, **132**, 154104.
- 32 L. Ma, J.-M. Zhang, K.-W. Xu and V. Ji, *Appl. Surf. Sci.*, 2015, **343**, 121–127.
- 33 W. Yang, H. Huang, X. Liu, J. Ren, K. Ma, Z. Pan, Z. Ding, X. Ding and Z. Gao, *Chem. Commun.*, 2020, **56**, 11657–11660.
- 34 G. Henkelman, A. Arnaldsson and H. Jónsson, *Comput. Mater. Sci.*, 2006, **36**, 354–360.
- 35 R. Dronskowski and P. E. Bloechl, *J. Phys. Chem.*, 1993, **97**, 8617–8624.
- 36 S. Maintz, V. L. Deringer, A. L. Tchougréeff and R. Dronskowski, *J. Comput. Chem.*, 2013, **34**, 2557–2567.
- 37 S. Maintz, V. L. Deringer, A. L. Tchougréeff and R. Dronskowski, *J. Comput. Chem.*, 2016, **37**, 1030–1035.
- 38 G. Henkelman and H. Jónsson, *J. Chem. Phys.*, 2000, **113**, 9978–9985.
- 39 G. Henkelman, B. P. Uberuaga and H. Jónsson, *J. Chem. Phys.*, 2000, **113**, 9901–9904.
- 40 A. Heyden, A. T. Bell and F. J. Keil, *J. Chem. Phys.*, 2005, **123**, 224101.
- 41 C. Riplinger and E. A. Carter, *J. Phys. Chem. C*, 2015, **119**, 9311–9323.
- 42 L. I. Bendavid and E. A. Carter, *J. Phys. Chem. C*, 2013, **117**, 26048–26059.
- 43 L. Zhao, Y. Zhang, L.-B. Huang, X.-Z. Liu, Q.-H. Zhang, C. He, Z.-Y. Wu, L.-J. Zhang, J. Wu, W. Yang, L. Gu, J.-S. Hu and L.-J. Wan, *Nat. Commun.*, 2019, **10**, 1278.
- 44 X. Liu, M. Xu, L. Wan, H. Zhu, K. Yao, R. Linguerri, G. Chambaud, Y. Han and C. Meng, *ACS Catal.*, 2020, **10**, 3084–3093.
- 45 Z. Song, B. Wang, J. Yu, C. Ma, T. Chen, W. Yang, S. Liu and L. Sun, *Chem. Eng. J.*, 2018, **354**, 517–524.
- 46 H. Li, C. Yan, H. Guo, K. Shin, S. M. Humphrey, C. J. Werth and G. Henkelman, *ACS Catal.*, 2020, **10**, 7915–7921.
- 47 J. P. Troutman, H. Li, A. M. Haddix, B. A. Kienzle, G. Henkelman, S. M. Humphrey and C. J. Werth, *ACS Catal.*, 2020, **10**, 7979–7989.
- 48 Y. Tang, W. Chen, J. Zhou, H. Chai, Y. Li, Y. Cui, Z. Feng and X. Dai, *Fuel*, 2019, **253**, 1531–1544.
- 49 B. Wang, Z. Song and L. Sun, *Chem. Eng. J.*, 2021, **409**, 128136.
- 50 W. Yang, Z. Gao, X. Liu, X. Li, X. Ding and W. Yan, *Catal. Sci. Technol.*, 2018, **8**, 4159–4168.
- 51 M. Gao, C. Cheng, Z. Miao, K. Wan and Q. He, *Energy*, 2023, **268**, 126657.
- 52 T. Bligaard, J. K. Nørskov, S. Dahl, J. Matthiesen, C. H. Christensen and J. Sehested, *J. Catal.*, 2004, **224**, 206–217.
- 53 W. Yang, X. Liu, X. Chen, Y. Cao, S. Cui, L. Jiao, C. Wu, C. Chen, D. Fu, I. D. Gates, Z. Gao and H.-L. Jiang, *Adv. Mater.*, 2022, **34**, 2110123.
- 54 S. Dong, J. Wang, C. Li, H. Liu, Z. Gao, C. Wu and W. Yang, *Appl. Surf. Sci.*, 2023, **609**, 155298.
- 55 H. Falsig, B. Hvolbæk, I. S. Kristensen, T. Jiang, T. Bligaard, C. H. Christensen and J. K. Nørskov, *Angew. Chem., Int. Ed.*, 2008, **47**, 4835–4839.
- 56 A. J. Medford, A. Vojvodic, J. S. Hummelshøj, J. Voss, F. Abild-Pedersen, F. Studt, T. Bligaard, A. Nilsson and J. K. Nørskov, *J. Catal.*, 2015, **328**, 36–42.
- 57 W. Yang, X. Chen, Y. Feng, F. Wang, Z. Gao, Y. Liu, X. Ding and H. Li, *Environ. Sci.: Nano*, 2022, **9**, 2041–2050.
- 58 Y. Tang, J. Zhou, W. Chen, H. Chai, Y. Li, Z. Feng and X. Dai, *Mol. Catal.*, 2019, **476**, 110524.

- 59 G. Cheng, B. Tan, Z. Zhang, S. Fu, W. Haiyan and F. Wang, *Fuel*, 2022, **315**, 123120.
- 60 X. Yan, Y. Li, C. Zhang, Y. Wang, J. Zhao and Z. Wang, *Fuel*, 2021, **303**, 121257.
- 61 W. Yang, B. Zhou, L. Chen, R. Shi, H. Li, X. Liu and Z. Gao, *Fuel*, 2023, **349**, 128751.
- 62 N. Daelman, M. Capdevila-Cortada and N. López, *Nat. Mater.*, 2019, **18**, 1215–1221.
- 63 S. Dong, C. Li, E. Lv, J. Wang, H. Liu, Z. Gao, W. Xiong, Z. Ding, W. Yang and H. Li, *J. Mater. Chem. A*, 2022, **10**, 19839–19851.
- 64 D. Cremer and E. Kraka, *Angew. Chem., Int. Ed. Engl.*, 1984, **23**, 627–628.
- 65 Z. Gao, Y. Sun, M. Li, W. Yang and X. Ding, *Appl. Surf. Sci.*, 2018, **456**, 351–359.